

WMAP¹ Polarization Results

A. Kogut²

The Wilkinson Microwave Anisotropy Probe (*WMAP*) has mapped the full sky in Stokes I , Q , and U parameters at frequencies 23, 33, 41, 61, and 94 GHz. We detect correlations between the temperature and polarization maps significant at more than 10 standard deviations. The correlations are inconsistent with instrument noise and are significantly larger than the upper limits established for potential systematic errors. Correlations on small angular scales are consistent with the signal expected from adiabatic initial conditions. We detect excess power on large angular scales consistent with an early epoch of reionization. A model-independent fit to reionization optical depth yields results consistent with the best-fit Λ CDM model, with best fit value $\tau = 0.17 \pm 0.04$ at 68% confidence, including systematic and foreground uncertainties.

1 Introduction

The Wilkinson Microwave Anisotropy Probe has mapped the full sky in the Stokes I , Q , and U parameters on angular scales $\theta > 0.2^\circ$ in 5 frequency bands centered at 23, 33, 41, 61, and 94 GHz (Bennett et al., 2003a). *WMAP* was not designed solely as a polarimeter, in the sense that none of its detectors are sensitive only to polarization. Incident radiation in each differencing assembly (DA) is split by an orthomode transducer (OMT) into two orthogonal linear polarizations (Page et al., 2003b; Jarosik et al., 2003). Each OMT is oriented so that the electric field directions accepted in the output rectangular waveguides lie at $\pm 45^\circ$ with respect to the yz symmetry plane of the satellite (see Bennett et al. (2003a) Fig. 2 for the definition of the satellite coordinate system). The two orthogonal polarizations from the OMT are measured by two independent radiometers. Each radiometer differences the signal in the accepted polarization between two positions on the sky (the A and B beams), separated by $\sim 140^\circ$.

The signal from the sky in each direction \hat{n} can be decomposed into the Stokes parameters

$$T(\hat{n}) = I(\hat{n}) + Q(\hat{n}) \cos 2\gamma + U(\hat{n}) \sin 2\gamma, \quad (1)$$

where we define the angle γ from a meridian through the Galactic poles to the projection on the sky of the E-plane of each output port of the OMT. Denoting the two radiometers by subscripts 1 and 2, the instantaneous outputs are

$$\begin{aligned} \Delta T_1 &= I(\hat{n}_A) + Q(\hat{n}_A) \cos 2\gamma_A + U(\hat{n}_A) \sin 2\gamma_A \\ &- I(\hat{n}_B) - Q(\hat{n}_B) \cos 2\gamma_B - U(\hat{n}_B) \sin 2\gamma_B \end{aligned} \quad (2)$$

¹WMAP is the result of a partnership between Princeton University and NASA's Goddard Space Flight Center. Scientific guidance is provided by the *WMAP* Science Team.

²Code 685, Goddard Space Flight Center, Greenbelt, MD 20771

and

$$\begin{aligned}\Delta T_2 &= I(\hat{n}_A) - Q(\hat{n}_A) \cos 2\gamma_A - U(\hat{n}_A) \sin 2\gamma_A \\ &\quad - I(\hat{n}_B) + Q(\hat{n}_B) \cos 2\gamma_B + U(\hat{n}_B) \sin 2\gamma_B.\end{aligned}$$

The sum

$$\Delta T_I \equiv \frac{1}{2}(\Delta T_1 + \Delta T_2) = I(\hat{n}_A) - I(\hat{n}_B) \quad (3)$$

is thus proportional to the unpolarized intensity, while the difference

$$\Delta T_P \equiv \frac{1}{2}(\Delta T_1 - \Delta T_2) = Q(\hat{n}_A) \cos 2\gamma_A + U(\hat{n}_A) \sin 2\gamma_A - Q(\hat{n}_B) \cos 2\gamma_B - U(\hat{n}_B) \sin 2\gamma_B. \quad (4)$$

is proportional only to the polarization. We produce full-sky maps of the Stokes I , Q , and U parameters from the sum and difference time-ordered data using an iterative mapping algorithm. Since the polarization is faint, the Q and U maps are dominated by instrument noise and converge rapidly (Hinshaw et al., 2003a).

The Stokes Q and U components depend on a specific choice of coordinate system. For each pair of pixels, we define coordinate-independent quantities

$$\begin{aligned}Q' &= Q \cos(2\phi) + U \sin(2\phi) \\ U' &= U \cos(2\phi) - Q \sin(2\phi),\end{aligned} \quad (5)$$

where the angle ϕ rotates the coordinate system about the outward-directed normal vector to put the meridian along the great circle connecting the two positions on the sky (Kamionkowski et al., 1997; Zaldarriaga & Seljak, 1997). All of our analyses use these coordinate-independent linear combinations of the Q and U sky maps.

2 CORRELATION FUNCTION

The simplest measure of temperature-polarization cross-correlation is the two-point angular correlation function

$$C^{IQ}(\theta) = \frac{\sum_{ij} I_i Q'_j w_i w_j}{\sum_{ij} w_i w_j}, \quad (6)$$

where i and j are pixel indices and w are the weights. To avoid possible effects of $1/f$ noise, we force the temperature map to come from a different frequency band than the polarization maps, and thus use the temperature map at 61 GHz (V band) for all correlations except the V-band polarization maps, which we correlate against the 41 GHz (Q band) temperature map. Since *WMAP* has a high signal-to-noise ratio measurement of the CMB temperature anisotropy, we use unit weight ($w_i = 1$) for the temperature maps and noise weight ($w_j = N_j/\sigma_0^2$) for the polarization maps, where N_j is the effective number of observations in each pixel j and σ_0 is the standard deviation of the white noise in the time-ordered data (Table 1 of Bennett et al. (2003b)). We compare the correlation functions to Monte Carlo simulations of a null model, which simulates the temperature anisotropy using the best-fit Λ CDM model

(Spergel et al., 2003) but forces the polarization signal to zero. Each realization generates a CMB sky in Stokes I , Q , and U parameters, convolves this simulated sky with the beam pattern for each differencing assembly, then adds uncorrelated instrument noise to each pixel in each map. We then co-add the simulated skies in each frequency band and compute $C^{IQ}(\theta)$ using the same software for both the *WMAP* data and the simulations. All analysis uses only pixels outside the *WMAP* Kp0 foreground emission mask (Bennett et al., 2003c), approximately 76% of the full sky.

Figure 1 shows $C^{IQ}(\theta)$ derived by co-adding the individual correlation functions for the frequencies 41, 61, and 94 GHz (Q, V, and W bands) least likely to be affected by Galactic foregrounds. The grey band shows the 68% confidence interval for the null simulations. It is clear that *WMAP* detects a temperature-polarization signal at high statistical confidence, and that signals exist on both large and small angular scales. We define a goodness-of-fit statistic

$$\chi^2 = \sum_{ab} [C_{\text{MAP}}^{IQ} - \langle C_{\text{sim}}^{IQ} \rangle]_a \mathbf{M}_{ab}^{-1} [C_{\text{MAP}}^{IQ} - \langle C_{\text{sim}}^{IQ} \rangle]_b, \quad (7)$$

where C_{MAP}^{IQ} is the co-added correlation function from *WMAP* data, $\langle C_{\text{sim}}^{IQ} \rangle$ is the mean from the Monte Carlo simulations, and \mathbf{M} is the covariance matrix between angular bins a and b derived from the simulations. We find $\chi^2 = 207$ for 78 degrees of freedom when comparing *WMAP* to the null model: *WMAP* detects temperature-polarization correlations significant at more than 10 standard deviations.

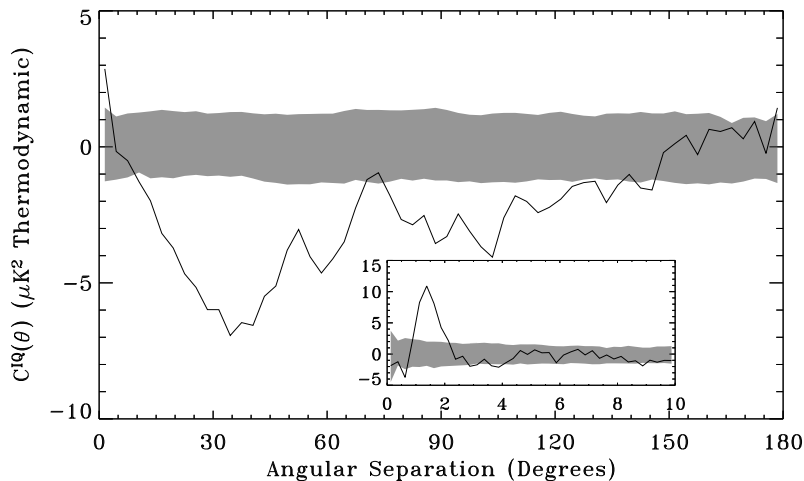


Figure 1: Temperature-polarization correlation function for *WMAP* co-added QVW data. The gray band shows the 68% confidence interval for similar co-added data taken from Monte Carlo simulations without polarization. The inset shows data for $\theta < 10^\circ$. The data are inconsistent with no temperature-polarization cross-correlations at more than 10 standard deviations. Note that the data are not independent between angular bins.

2.1 Systematic Error Analysis

Having detected a significant signal in the data, we must determine whether this signal has a cosmological origin or results from systematic errors or foreground sources. We test the convergence of the mapping algorithm using end-to-end simulations, comparing maps derived from simulated time-ordered data to the input maps used to generate the simulated time series. The simulations include all major instrumental effects, including beam ellipticity, radiometer performance, and instrument noise (including $1/f$ component), and are processed using the same map-making software as the *WMAP* data (Hinshaw et al., 2003a). The Q and U maps converge rapidly, within the 30 iterations required to derive the calibration solution. Correlations in the time-ordered data introduce an anti-correlation in the U map at angles corresponding to the beam separation, with amplitude 0.5% of the noise in the map. This effect is independent for each radiometer and does not affect temperature-polarization cross-correlations. Similarly, residual $1/f$ noise in the time series can create faint striping in the maps, but does not affect cross-correlations.

The largest potential systematic error in the temperature-polarization cross-correlation results from bandpass mismatches in the amplification/detection chains. We calibrate the *WMAP* data in thermodynamic temperature using the Doppler dipole from the satellite’s orbit about the Sun as a beam-filling calibration source (Hinshaw et al., 2003a). Astrophysical sources with a spectrum other than a 2.7 K blackbody are thus slightly mis-calibrated. The amplitude is dependent on the product of the source spectrum with the unique bandpass of each radiometer. If the bandpasses in each radiometer were identical, the effect would cancel for any frequency spectrum, but differences in the bandpasses between the two radiometers in each DA generate a non-zero residual in the difference signal used to generate polarization maps (Eq. 4). This signal is spatially correlated with the unpolarized foreground intensity but is independent of the orientation of the radiometers on the sky (polarization angle γ). In the limit of uniform sampling of γ this term drops out of the sky map solution. However, the *WMAP* scan pattern does not view each pixel in all orientations; unpolarized emission with a non-CMB spectrum can thus be aliased into polarization if the bandpasses of the two radiometers in each DA are not identical. This is a significant problem only at 23 GHz (K band), where the foregrounds are brightest and the bandpass mismatch is largest.

We quantify the effect of bandpass mismatch using end-to-end simulations. For each time-ordered sample, we compute the signal in each radiometer using an unpolarized foreground model and the measured pass bands in each output channel (Jarosik et al., 2003). We then generate maps from the simulated data using the *WMAP* one-year sky coverage and compute $C^{IQ}(\theta)$ using the output I , Q , and U maps from the simulation. We treat this as an angular template and compute the least-squares fit of the *WMAP* data to this bandpass template to determine the amplitude of the effect in the observed correlation functions. We correct the *WMAP* correlation functions $C^{IQ}(\theta)$ and $C^{IU}(\theta)$ at K and Ka bands by subtracting the best-fit template amplitudes. The fitted signal has peak amplitude of $8 \mu\text{K}^2$ at 23 GHz and $5 \mu\text{K}^2$ at 33 GHz. No other channel has a statistically significant detection of this effect.

Sidelobe pickup of polarized emission from the Galactic plane can also produce spu-

rious polarization at high latitudes in the Q and U maps. We estimate this effect using the measured far-sidelobe response for each beam in each polarization (Barnes et al., 2003). Sidelobe pickup of polarized structure in the Galactic plane is less than $1 \mu\text{K}^2$ in $C^{IQ}(\theta)$ at 23 GHz and below $0.1 \mu\text{K}^2$ in all other bands. We correct the polarization maps for the estimated sidelobe signal and propagate the associated systematic uncertainty throughout our analysis. Note that all of these systematic errors depend on the Galactic foregrounds, and have different frequency dependence than CMB polarization.

Other instrumental effects are negligible. We measure polarization by differencing the outputs of the two radiometers in each differencing assembly (Eq. 4). Calibration errors (as opposed to the bandpass effect discussed above) can alias temperature anisotropy into a spurious polarization signal. We have simulated the uncertainty in the calibration solution using both realistic gain drifts and drifts ten times larger than observed in flight (Hinshaw et al., 2003a). Gain drifts (either intrinsic or thermally-induced) contribute less than $1 \mu\text{K}^2$ to $C^{IQ}(\theta)$ in the worst band.

Null tests provide an additional check for systematic errors. Thomson scattering of scalar temperature anisotropy produces a curl-free polarization pattern. A non-zero cosmological signal is thus expected only for the IQ (TE) correlation, whereas systematic errors or foreground sources can affect both the IQ and IU (TB) correlations. A χ^2 analysis shows $C^{IU}(\theta)$ to be consistent with instrument noise. We further limit possible systematic effects by correlating the Stokes I sum map from the Q- or V-band (as noted above) with the polarization *difference* maps $(Q1 - Q2)/2$, $(V1 - V2)/2$, $(W1 - W2)/2$, and $(W3 - W4)/2$. The temperature (Stokes I) map in all cases is a sum map; the test is thus primarily sensitive to systematic errors in the polarization data. The difference maps are consistent with instrument noise.

2.2 Foregrounds

Galactic emission is not a strong contaminant for CMB temperature anisotropy, but could be significant in polarization. *WMAP* measurements of unpolarized foreground emission show synchrotron, free-free, and thermal dust emission all sharing significant spatial structure. Of these components, only synchrotron emission is expected to generate significant polarization; other sources such as spinning dust are limited to less than 5% of the total intensity at 33 GHz (Bennett et al., 2003c).

Foreground polarization above 40 GHz is faint: fitting the correlation functions at 41, 61, and 94 GHz (Q, V, and W bands) to a single power-law $C^{IQ}(\theta, \nu) = C_0^{IQ}(\theta) (\nu/\nu_0)^\beta$ yields spectral index $\beta = -0.4 \pm 0.4$, consistent with a CMB signal ($\beta = 0$) and inconsistent with the spectral indices expected for synchrotron ($\beta \approx -3$), spinning dust ($\beta \approx -2$), or thermal dust ($\beta \approx 2$). The measured signal can not be produced solely by a single foreground emission component.

A two-component fit

$$C^{IQ}(\theta, \nu) = C_{\text{CMB}}^{IQ}(\theta) + C_{\text{Gal}}^{IQ}(\theta) \left(\frac{\nu}{\nu_0} \right)^\beta \quad (8)$$

tests for the superposition of a CMB component with a single foreground component. Figure 2 shows the resulting decomposition into CMB and foreground components. We obtain a marginal detection of foreground component with best-fit spectral index $\beta = -3.7 \pm 0.8$ consistent with synchrotron emission. We test for consistency or possible residual systematic errors by repeating the fit using different temperature maps and different combinations of *WMAP* polarization channels. The fitted CMB component (left panels of Fig. 2) is robust against all combinations of frequency channels and fitting techniques. Note the agreement in Fig. 2 between nearly independent data sets: the co-added QVW data (uncorrected for foreground emission) and the KKaQ data (corrected for foreground emission). We obtain additional confirmation by replacing the V-band temperature map in the cross-correlation (Eq. 6) with the “internal linear combination” temperature map designed to suppress foreground emission (Bennett et al., 2003c). The fitted CMB component does not change. We test for systematic errors by replacing the temperature map with the COBE-DMR map of the

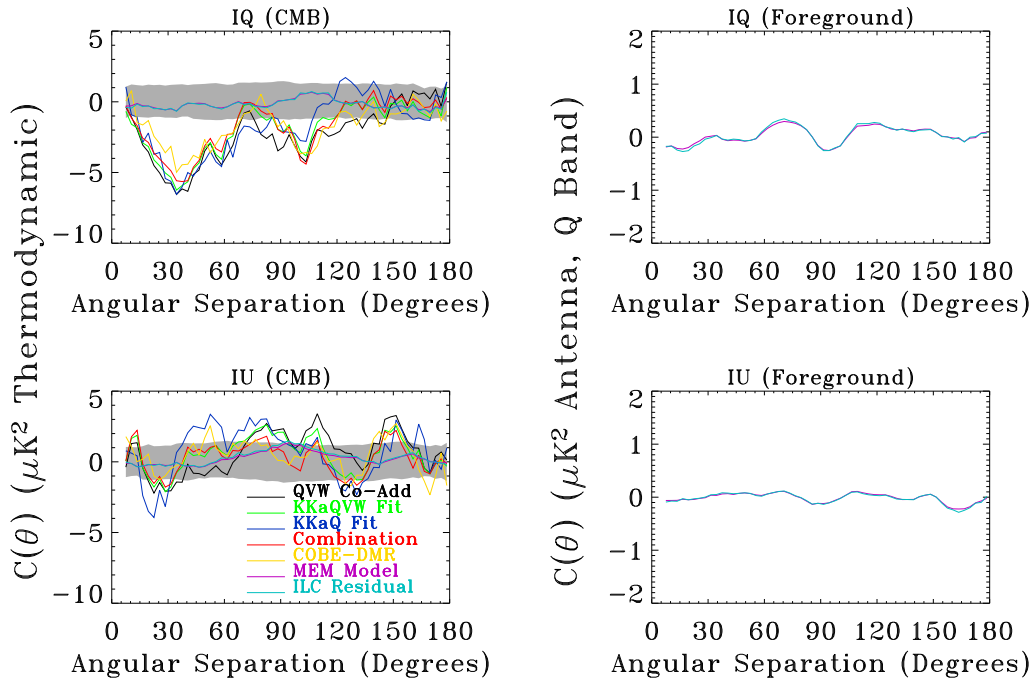


Figure 2: Fitted CMB (left) and foreground (right) components from a multi-frequency decomposition of the measured two-point correlation functions. Top panels show the IQ (TE) correlation, while bottom panels show IU (TB). The CMB component is shown in units of thermodynamic temperature, while the foreground is shown in antenna temperature evaluated at 41 GHz. Different colors show the effect of using different temperature maps in the cross-correlation, or including different polarization frequency channels in the CMB-foreground decomposition (see text). The fitted CMB component is stable as different frequency channels and data sets are analyzed. Foreground emission is faint compared to the cosmic signal.

CMB temperature (Bennett et al., 1996), excluding *any* instrumental correlation between the temperature and polarization data. Again, the results are unchanged.

We further constrain foreground contributions by computing the cross-correlation between the *WMAP* polarization data and temperature maps dominated by foregrounds. We replace the temperature map in Eq. 6 with either the *WMAP* maximum-entropy foreground model (Bennett et al., 2003c) or a “residual” foreground map created by subtracting the internal linear combination CMB map from the individual *WMAP* temperature maps. We then correlate the foreground temperature map against the *WMAP* polarization data in each frequency band, and fit the resulting correlation functions to CMB and foreground components (Eq. 8). The two foreground maps provide nearly identical results. The fitted CMB component has nearly zero amplitude, consistent with the instrument noise. The fitted foreground has amplitude $0.5 \pm 0.1 \mu\text{K}^2$ at $\nu_0 = 41$ GHz, with best-fit index $\beta = -3.4$ consistent with synchrotron emission.

3 POLARIZATION CROSS-POWER SPECTRA

In a second analysis method, we compute the angular power spectrum of the temperature-polarization correlations using a quadratic estimator (*cf* Appendix A in Kogut et al. (2003)). We compute c_l^{TE} and c_l^{TB} individually for the each *WMAP* frequency band, using uniform weight for the temperature map and noise weight for the polarization maps. We then combine the angular power spectra, using noise-weighted QVW data for $l > 21$ where foregrounds are insignificant, and a fit to CMB plus foregrounds using all 5 frequency bands for $l \leq 21$. Since foreground contamination is weak, we gain additional sensitivity in this analysis by using the Kp2 sky cut retaining 85% of the sky.

We estimate the uncertainty in each l bin using the covariance matrix \mathbf{M} for the polarization cross-power spectrum. Based on our analysis of the c_l^{TT} covariance matrix (Hinshaw et al., 2003b), the c_l^{TE} covariance matrix has the form along the diagonal of

$$\mathbf{M}_{ll} = \langle c_l^{TE} c_l^{TE} \rangle - \langle c_l^{TE} \rangle^2 \quad (9)$$

$$\simeq \frac{(c_l^{TT} + n_{TT}/w_l)(c_l^{EE} + n_{EE}/w_l) + (c_l^{TE})^2}{(2l+1)f_{sky}f_{sky}^{\text{eff}}} \quad (10)$$

where n_{TT} and n_{EE} are the TT and EE noise bias terms, w_l is the effective window function for the combined maps (Page et al., 2003a), c_l^{TT} and c_l^{EE} are the temperature and polarization angular power spectra, $f_{sky} = 0.85$ is the fractional sky coverage for the Kp2 mask, and $f_{sky}^{\text{eff}} = f_{sky}/1.14$ for noise weighting. We take the c_l^{TT} term from the measured temperature power spectra (Hinshaw et al., 2003b) and the c_l^{EE} term predicted by the best-fit Λ CDM model (Spergel et al., 2003) (allowing c_l^{EE} to vary as a function of optical depth in the likelihood analysis). Monte Carlo simulations demonstrate that the analytic expression accurately describes the diagonal elements of the covariance matrix. We approximate the off-diagonal terms using the geometric mean of the covariance matrix terms for uniform and

noise weighting (Hinshaw et al., 2003b),³

$$\mathbf{M}_{ll'} \simeq (\mathbf{M}_{ll} \mathbf{M}_{l'l'})^{0.5} r_{\Delta l}. \quad (11)$$

The largest off-diagonal contribution, -2.8% , is at $\Delta l = 2$ from the symmetry of our sky cut and noise coverage. The total anticorrelation is $\sum_{\Delta l \neq 0} r_{\Delta l} = -0.124$. Because of this anti-correlation, the error bars for the binned c_l^{TE} are slightly smaller than the naive estimate.

Figure 3 shows the polarization cross-power spectra for the *WMAP* one-year data. The solid line shows the predicted signal for adiabatic CMB perturbations, based only on a fit to the measured temperature angular power spectrum c_l^{TT} (Spergel et al., 2003; Hinshaw et al., 2003b). Two features are apparent. The TE data on degree angular scales ($l > 20$) are in excellent agreement with *a priori* predictions of adiabatic models (Coulson et al., 1994). Other than the specification of adiabatic perturbations, there are no free parameters – the solid line is not a fit to c_l^{TE} . The χ^2 of 24.2 for 23 degrees of freedom indicates that the CMB anisotropy is dominated by adiabatic perturbations. On large angular scales ($l < 20$) the data show excess power compared to adiabatic models, suggesting significant reionization.

The *WMAP* detection of the acoustic structure in the TE spectrum confirms several basic elements of the standard paradigm. The amplitudes of the peak and anti-peak are a measure of the thickness of the decoupling surface, while the shape confirms the assumption

³Note that Hinshaw et al. (2003b) define off-diagonal elements in terms of the inverse covariance matrix, which differs from $r_{\Delta l}$ by a sign.

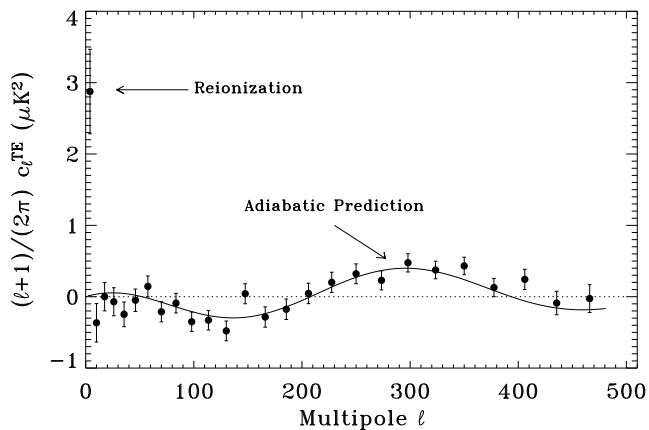


Figure 3: Polarization cross-power spectra c_l^{TE} for the *WMAP* one-year data. Note that we plot $(l+1)/2\pi c_l^{TE}$ and not $l(l+1)/2\pi c_l^{TE}$. This choice emphasizes the oscillatory nature of c_l^{TE} . For clarity, the dotted line shows $c_l = 0$. The solid line is the predicted signal based on the c_l^{TT} power spectrum of temperature anisotropy – there are no free parameters. The TE correlation on degree angular scales ($l > 20$) is in excellent agreement with the signal expected from adiabatic CMB perturbations. The excess power at low l indicates significant reionization at large angular scales.

that the primordial fluctuations are adiabatic. Adiabatic fluctuations predict a temperature/polarization signal anticorrelated on large scales, with TE peaks and anti-peaks located midway between the temperature peaks Hu & Sugiyama (1994). The existence of TE correlations on degree angular scales also provides evidence for super-horizon temperature fluctuations at decoupling, as expected for inflationary models of cosmology (Peiris et al., 2003)

4 REIONIZATION

WMAP detects statistically significant correlations between the CMB temperature and polarization. The signal on degree angular scales ($l > 20$) agrees with the signal expected in adiabatic models based solely on the temperature power spectrum, without any additional free parameters. We also detect power on large angular scales ($l < 10$) well in excess of the signal predicted by the temperature power spectrum alone. This signal can not be explained by data processing, systematic errors, or foreground polarization, and has a frequency spectrum consistent with a cosmological origin.

The signal on large angular scales has a natural interpretation as the signature of early reionization. Both the temperature and temperature-polarization power spectra can be related to the power spectrum of the radiation field during scattering (Zaldarriaga, 1997). Thomson scattering damps the temperature anisotropy and regenerates a polarized signal on scales comparable to the horizon. The existence of polarization on scales much larger than the acoustic horizon at decoupling implies significant scattering at more recent epochs.

4.1 Reionization in a Λ CDM Universe

If we assume that the Λ CDM model is the best description of the physics of the early universe, we can fit the observed temperature-polarization cross-power spectrum to derive the optical depth τ . We assume a step function for the ionization fraction x_e and use the CMBFAST code (Seljak & Zaldarriaga, 1996) to predict the multipole moments as a function of optical depth. While this assumption is simplistic, our conclusions on optical depth are not very sensitive to details of the reionization history or the background cosmology.

Figure 4 compares the polarization cross-power spectrum c_l^{TE} derived from the quadratic estimator to Λ CDM models with and without reionization. The rise in power for $l < 10$ is clearly inconsistent with no reionization. We quantify this using a maximum-likelihood analysis

$$\mathcal{L} \propto \frac{\exp(-\frac{1}{2}\chi^2)}{|\mathbf{M}|^{1/2}}. \quad (12)$$

Figure 5 shows the relative likelihood $\mathcal{L}/\text{Max}(\mathcal{L})$ for the optical depth τ assuming a Λ CDM cosmology, with all other parameters fixed at the values derived from the temperature power spectrum alone (Spergel et al., 2003). The likelihood for the 5-band data corrected for foreground emission peaks at $\tau = 0.17 \pm 0.03$ (statistical error only): *WMAP* detects the signal from reionization at high statistical confidence.

A full error analysis for τ must account for systematic errors and foreground uncertainties. We propagate these effects by repeating the maximum likelihood analysis using different combinations of *WMAP* frequency bands and different systematic error corrections. We correct $C^{IQ}(\theta)$ in each frequency band not for the best estimate of the systematic error templates, but rather the best estimate plus or minus one standard deviation. We then fit the mis-corrected $C^{IQ}(\theta, \nu)$ for a CMB piece plus a foreground piece (Eq. 8) and use the CMB piece in a maximum-likelihood analysis for τ . The change in the best-fit value for τ as we vary the systematic error corrections propagates the uncertainties in these corrections. Systematic errors have a negligible effect on the fitted optical depth; altering the systematic error corrections changes the best-fit values of τ by less than 0.01.

The largest non-random uncertainty is the foreground separation. We assess the uncertainty in the foreground separation by repeating the entire systematic error analysis (using both standard and altered systematic error corrections) with the foreground spectral index $\beta = -3.7 \pm 0.8$ shifted one standard deviation up or down from the best-fit value. Fitted values for τ derived from the three high-frequency channels (QVW) without foreground fitting are in agreement with lower-frequency data once foregrounds are taken into account. We obtain nearly identical values for τ when fitting either the highest-frequency data set QVW or the lowest-frequency set KKaQ. The fitted optical depth is insensitive to the spectral index: varying the spectral index from -2.9 to -4.5 changes the fitted values by 0.02 or less. We adopt $\tau = 0.17 \pm 0.04$ as the best estimate for the optical depth to reionization, where the error bar reflects a 68% confidence level interval including statistical, systematic, and foreground uncertainties.

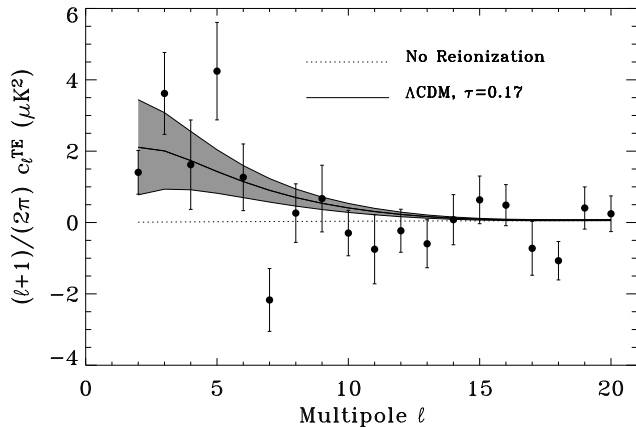


Figure 4: *WMAP* Polarization cross-power spectra c_l^{TE} (filled circles) compared to Λ CDM models with and without reionization. The rise in power for $l < 10$ is consistent with reionization optical depth $\tau = 0.17 \pm 0.04$. The error bars on *WMAP* data reflect measurement errors only; adjacent points are slightly anti-correlated. The grey band shows the 68% confidence interval from cosmic variance. The value at $l = 7$ is particularly sensitive to the foreground correction.

Spergel et al. (2003) include the TE data in a maximum-likelihood analysis combining *WMAP* data with other astronomical measurements. The resulting value, $\tau = 0.17 \pm 0.06$, is consistent with the value derived from the TE data alone. The larger uncertainty reflects the effect of simultaneously fitting multiple parameters. The TE analysis propagates foreground uncertainties by re-evaluating the likelihood using different foreground spectral index. Since foreground affect only the lowest multipoles, the combined analysis propagates foreground uncertainty by doubling the statistical uncertainty in c_l^{TE} for $2 \leq l \leq 4$ to account for this effect.

4.2 Model-Independent Estimate

An alternative approach avoids assuming any cosmological model and uses the measured temperature angular correlation function to determine the radiation power spectrum at recombination. This approach assumes that the best estimate of the three dimensional radiation power spectrum is the *measured* angular power spectrum rather than a model fit to the angular power spectrum. Given the observed temperature power spectrum c_l^{TT} , we derive the predicted polarization cross-power spectrum c_l^{TE} , which we then fit to the observed TE spectrum as a function of optical depth τ . We obtain $\tau = 0.16 \pm 0.04$, in excellent agreement with the value derived assuming a Λ CDM cosmology. We emphasize that the model-independent technique makes *no* assumptions about the cosmology. The fact that it agrees well with the best-fit model from the combined temperature and polarization data (Spergel et al., 2003) is an additional indication that the observed temperature-polarization correlations on large angular scales represent the imprint of physical conditions at reionization. The dependence on the underlying cosmology is small.

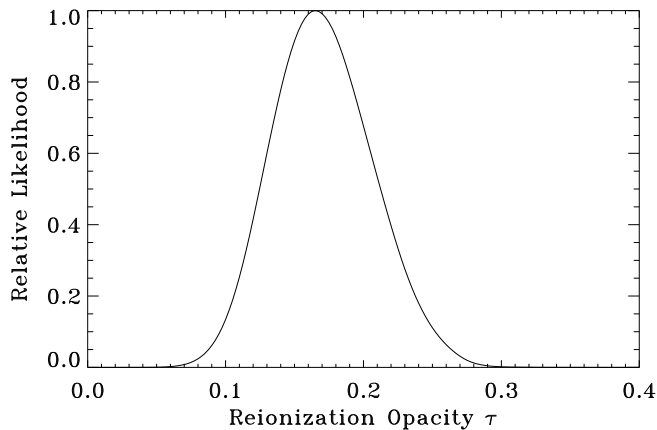


Figure 5: Likelihood function for optical depth τ for a Λ CDM cosmology, using all 5 *WMAP* frequency bands fitted to CMB plus foregrounds with foreground spectral index $\beta = -3.7$. After including systematic and foreground uncertainties the optical depth is consistent with a value $\tau = 0.17$ with 95% confidence range $0.09 \leq \tau \leq 0.28$.

4.3 Early Star Formation

Reionization can also be expressed as a redshift z_r assuming an ionization history. We consider two simple cases. For instantaneous reionization with ionization fraction $x_e = 1$ at $z < z_r$, the measured optical depth corresponds to redshift $z_r = 17 \pm 3$. This conflicts with measurements of the Gunn-Peterson absorption trough in spectra of distant quasars, which show neutral hydrogen present at $z \approx 6$ (Becker, 2001; Djorgovski et al., 2001; Fan, 2002). Reionization clearly did not occur through a single rapid phase transition. However, since absorption spectra are sensitive to even small amounts of neutral hydrogen, models with partial ionization $x_e \lesssim 1$ can have enough neutral column density to produce the Gunn-Peterson trough while still providing free electrons to scatter CMB photons and produce large-scale polarization. Direct Gunn-Peterson observations only imply a neutral hydrogen fraction $\gtrsim 1\%$ (Fan, 2002). Accordingly, we modify the simplest model to add a second transition: a jump from $x_e = 0$ to $x_e = 0.5$ at redshift z_r , followed by a second transition from $x_e = 0.5$ to $x_e = 1$ at redshift $z = 7$. Fitting this model to the measured optical depth yields $z_r \approx 20$. In reality, reionization is more complicated than simple step transitions. Allowing for model uncertainty, the measured optical depth is consistent with reionization at redshift $11 < z_r < 30$, corresponding to times $100 < t_r < 400$ Myr after the Big Bang (95% confidence).

Extrapolations of the observed ionizing flux to higher redshift lead to predicted CMB optical depth between $0.04 - 0.08$ (Miralda-Escude, 2002), lower than our best fit values. The measured optical depth thus implies additional sources of ionizing flux at high redshift. An early generation of very massive (Pop III) stars could provide the required additional heating. Tegmark (1997) estimate that 10^{-3} of all baryons should be in collapsed objects by $z = 30$. If these baryons form massive stars, they would reionize the universe. However, photons below the hydrogen ionization threshold will destroy molecular hydrogen (the principal vehicle for cooling in early stars), driving the effective mass threshold for star formation to $\sim 10^8$ solar masses and impeding subsequent star formation (Haiman et al., 1997; Gnedin & Ostriker, 1997; Tegmark, 1997). X-ray heating and ionization (Venkatesan et al., 2001; Oh, 2001) may provide a loophole to this argument by enhancing the formation of H_2 molecules (Haiman et al., 2000).

Cen (2003) provides a physically-motivated model of “double reionization” that resembles the two-step model above. A first generation of massive Pop III stars initially ionizes the intergalactic medium. The increased metallicity of the intergalactic medium then produces a transition to smaller Pop II stars, after which the reduced ionizing flux allows regeneration of a neutral hydrogen fraction. The ionization fraction remains at $x_e \approx 0.6$ until the global star formation rate surpasses the recombination rate at $z = 6$, restoring $x_e = 1$. The predicted value $\tau = 0.10 \pm 0.03$ should be increased somewhat to reflect the higher *WMAP* values for the baryon density Ω_b and normalization σ_8 (Spergel et al., 2003). The contribution from ionized helium will also serve to increase τ (Venkatesan et al., 2003; Wyithe & Loeb, 2003). The *WMAP* determination of the optical depth indicates that ionization history must be more complicated than a simple instantaneous step function. While physically plausible models can reproduce the observed optical depth, reionization remains

a complex process and can not be fully characterized by a single number. A more complete determination of the ionization history requires evaluation of the detailed TE and EE power spectra (Kaplinghat et al., 2003; Hu & Holder, 2003).

The *WMAP* mission is made possible by the support of the Office of Space Sciences at NASA Headquarters and by the hard and capable work of scores of scientists, engineers, technicians, machinists, data analysts, budget analysts, managers, administrative staff, and reviewers.

References

Barnes, C. et al. 2003, ApJ in press

Becker, R. H. e. a. 2001, AJ, 122, 2850

Bennett, C. L., Bay, M., Halpern, M., Hinshaw, G., Jackson, C., Jarosik, N., Kogut, A., Limon, M., Meyer, S. S., Page, L., Spergel, D. N., Tucker, G. S., Wilkinson, D. T., Wollack, E., & Wright, E. L. 2003a, ApJ, 583, 1

Bennett, C. L., Halpern, M., Hinshaw, G., Jarosik, N., Kogut, A., Limon, M., Meyer, S. S., Page, L., Spergel, D. N., Tucker, G. S., Wollack, E., Wright, E. L., Barnes, C., Greason, M., Hill, R., Komatsu, E., Nolta, M., Odegard, N., Peiris, H., Verde, L., & Weiland, J. 2003b, ApJ, in press

Bennett, C. L. et al. 2003c, ApJ, in press

Bennett, C. L., Banday, A. J., Górski, K. M., Hinshaw, G., Jackson, P., Keegstra, P., Kogut, A., Smoot, G. F., Wilkinson, D. T., & Wright, E. L. 1996, ApJl, 464, L1

Cen, R. 2003, ApJ, submitted (astro-ph/0210473)

Coulson, D., Crittenden, R. G., & Turok, N. G. 1994, PRL, 73, 2390

Djorgovski, S. G., Castro, S., Stern, D., & Mahabal, A. A. 2001, ApJl, 560, L5

Fan, X. e. a. 2002, AJ, 123, 1247

Gnedin, N. Y. & Ostriker, J. P. 1997, ApJ, 486, 581

Haiman, Z., Abel, T., & Rees, M. J. 2000, ApJ, 534, 11

Haiman, Z., Rees, M. J., & Loeb, A. 1997, ApJ, 484, 985

Hinshaw, G. F. et al. 2003a, ApJ, in press

—. 2003b, ApJ, in press

Hu, W. & Holder, G. P. 2003, PRD, submitted (astro-ph/0303400)

Hu, W. & Sugiyama, N. 1994, ApJ, 436, 456

Jarosik, N. et al. 2003, ApJs, 145

Kamionkowski, M., Kosowsky, A., & Stebbins, A. 1997, PRD, 55, 7368

Kaplinghat, M., Chu, M., Haiman, Z., Holder, G. P., Knox, L., & Skordis, C. 2003, ApJ, 583, 24

Kogut, A. et al. 2003, ApJ, astro-ph/0302213

Miralda-Escude, J. 2002, ApJ, submitted (astro-ph/0211071)

Oh, S. P. 2001, ApJ, 553, 499

Page, L. et al. 2003a, ApJ, in press

—. 2003b, ApJ, 585, in press

Peiris, H. et al. 2003, ApJ, in press

Seljak, U. & Zaldarriaga, M. 1996, ApJ, 469, 437

Spergel, D. N. et al. 2003, ApJ, in press

Tegmark, M., e. a. 1997, ApJ, 474, 1

Venkatesan, A., Tumlinson, J., & Shull, J. M. 2003, ApJ, 584, 621

Venkatesan, A., Giroux, M. L., & Shull, J. M. 2001, ApJ, 563, 1

Wyithe, J. S. B. & Loeb, A. 2003, ApJ, 586, 693

Zaldarriaga, M. 1997, PRD, 55, 1822

Zaldarriaga, M. & Seljak, U. 1997, PRD, 55, 1830